Microwave Radiances from Precipitating Clouds Containing Aspherical Ice, Combined Phase, and Liquid Hydrometeors

RONGZHANG WU[1] AND J. A. WEINMAN

Space Science and Engineering Center, University of Wisconsin

Microwave radiances have been computed as a function of rainfall rates from precipitating clouds containing ice, combined phase, and water hydrometeors. The ice at the top of the precipitating cloud depresses the brightness temperatures by reflecting radiances that emerge from the liquid hydrometeors at lower altitudes. Because the density of ice hydrometeors is related to the rainfall rate at the surface, the brightness temperatures are sensitive to large rainfall rates. The solution of the transfer equation considers the vertically inhomogeneous structure of the precipitation as well as the polarized emissivity of the underlying surface. The altitudes from which radiances derive their energy are presented for several rainfall profiles and frequencies. It is shown that the lower-frequency radiances are sensitive to liquid precipitation at low altitudes while the higher-frequency radiances are more sensitive to the ice hydrometeors at the cloud tops. The extinction coefficients of aspherical hydrometeors are presented as a function of rainfall rates. Measurements at 37.0-GHz microwave radiances from Nimbus 7 suggest that the vertically polarized radiances are 12 ± 2°K warmer than the horizontally polarized radiances at high rainfall rates. This difference diminishes at lower frequencies. The present model reveals that such effects can be traced to aspherical ice hydrometeors in the upper regions of precipitating clouds.

1. INTRODUCTION

Numerous models of the transfer of microwave radiation in rain have been developed during the past years, see *Atlas and Theile* [1981] and *Huang and Liou* [1983]. These models have primarily derived radiances emerging from clouds of spherical raindrops uniformly distributed in height. Several phenomena not considered in these earlier models have recently become evident from the data obtained from the Scanning Multichannel Microwave Radiometer (SMMR) on the Nimbus 7 satellite:

Spencer et al. [1983a] used data from SMMR to measure rainfall rates up to 90 mm/h over land. This technique relied upon the fact that heavy precipitation is frequently associated with a significant quantity of frozen hydrometeors. The frozen hydrometeors reflect microwave radiances emitted by the raindrops below the ice so that the brightness temperature measured from space is reduced in proportion to the rainfall rate. This observation is in contrast with results predicted by earlier radiative transfer models that neglected the effect of frozen hydrometeors. Those models yielded 37-GHz brightness temperatures that became insensitive to increases in rainfall rates in excess of 20 mm/h. Defense Meteorological Satellite Program (DMSP) radiometers on the Special Sensor Microwave/Imager (SSM/I) of the future DMSP satellite will measure radiances at 85.6 GHz as well as at 37, 21, and 19 GHz. *Wilheit et al.* [1982] has shown that the 92-GHz radiances are especially sensitive to the presence of ice hydrometeors. The microwave radiative transfer model presented in this study includes the effect of liquid, combined phase, and ice hydrometeors in the same storm system on the radiances escaping to space.

The 37-GHz data from SMMR obtained by *Spencer et al.* [1983a, b] also indicated that differences in the brightness temperatures emerging from intense storms, measured with vertical and horizontal polarization at a zenith angle of 50°,

remained in excess of 12 ± 2°K. This residual temperature difference cannot be derived from radiative transfer models that only consider the effect of spherical raindrops, see *Weinman and Guetter* [1977] and *Huang and Liou* [1983]. It is suggested that this residual temperature difference might be caused by aspherical hydrometeors. *Bostian and Allnutt* [1979] and *Oguchi* [1983] summarized microwave communication studies that showed that hydrometeors are indeed deformed and that their electromagnetic properties differ from those of spherical particles. The following microwave radiative transfer model will also include the effects of hydrometeor deformation on the microwave radiances emitted to space.

2. THEORY

2a. Radiative Transfer Model

We will consider the transfer of horizontally and vertically polarized radiances I_h and I_v, respectively, through a stratified cloud of hydrometeors whose structure, phase, and temperature varies only in the vertical coordinate z, whose origin is at the surface. It will become evident that profiles of the concentration, phase, shape, and size of the hydrometeors exert a significant influence on these radiances. Unfortunately, these parameters are not generally known, so that a rigorous mathematical analysis of the radiative transfer equation is not justified. Thus these radiances will be determined by Eddington's second approximation to the equation of radiative transfer based on the study of *Weinman and Davies* [1978]:

$$\cos \theta \frac{dI_p}{dz} = -k_p(I_p - J) \tag{1}$$

where p is h or v for the horizontally or vertically polarized radiances, respectively. The extinction coefficient $k_p(z)$ is appropriate to the polarization p.

The source term is

$$J(z, \theta, \phi) = [1 - \bar{a}(z)]T(z) + \frac{\bar{a}(z)}{4\pi} \int_0^{2\pi} \int_{-1}^{1} \bar{P}(\theta, \phi; \theta', \phi')$$
$$\cdot \bar{I}(z, \theta', \phi')d(\cos \theta') \, d\phi' \tag{2}$$

where $\bar{a}(z)$ is the albedo for single scattering of an ensemble of spherical particles whose volume is equal to that of the as-

Permanent address: Central Meteorological Bureau, Beijing, People's Republic of China.

pherical particles, $\bar{P}(\theta, \phi; \theta', \phi')$ is the phase function of the equivalent spherical particles that describes scattering from zenith angle θ' to θ and azimuth angle ϕ' to ϕ, and $\bar{I}(z, \theta', \phi')$ is the diffuse radiance averaged over both polarizations incident on the scattering volume from zenith angle θ' and azimuth angle ϕ'. The Planck blackbody function is represented as an equivalent brightness temperature $T(z)$ by the Rayleigh-Jeans approximation at microwave frequencies.

The model considers precipitation hydrometeors of various phases and shapes, which scatter and absorb radiation, and O_2 and H_2O vapor, which only absorb radiation. A simplification of (1) assumes that absorption rather than scattering is the dominant extinction mechanism for frequencies less than or equal to 37 GHz for liquid hydrometeors. The liquid hydrometeors are assumed to be oblate ellipsoids with the radiative properties presented by *Oguchi and Hosoya* [1974]. It is also assumed that ice hydrometeors are ellipsoidal in shape and oriented so that their large dimensions are horizontal, in accord with the accounts of *Prupacher and Klett* [1980] and *Bostian and Allnutt* [1979].

The solution to (1) is sought iteratively. A source function is first derived from the Eddington approximation in which it is assumed that the hydrometeors are spherical. That approximate source function and the extinction coefficients for aspherical hydrometeors are then introduced into the equations that define the radiances. We initially assume that the unpolarized radiance can be represented by an azimuthally independent radiance in accord with Eddington's approximation, see *Liou* [1980]:

$$\bar{I}(z, \theta, \phi) = I_0(z) + I_1(z) \cos \theta \tag{3}$$

and the phase function is approximated by

$$\bar{P}(\theta, \phi; \theta', \phi') = 1 + 3\bar{g}(z)$$
$$\cdot [\cos \theta' \cdot \cos \theta + \sin \theta' \cdot \sin \theta \cos (\phi' - \phi)] \tag{4}$$

where $\bar{g}(z)$ is the asymmetry factor of the phase function for spherical particles whose volume is the same as the apherical particles.

While it has been noted that radiances, temperature profiles, extinction coefficients, albedoes for single scattering, and asymmetry factors all vary with heights, we will no longer indicate this dependence explicitly in the subsequent discussion.

Inserting (3) and (4) into (2) yields

$$J = [1 - \bar{a}]T + \bar{a}[I_0 + \bar{g}I_1 \cos \theta] \tag{5}$$

Integrating (1) with respect to $\cos \theta$ $d(\cos \theta)$ and $d\phi$ over $-1 \le \cos \theta \le 1$ and $0 \le \phi \le 2\pi$ yields

$$\frac{dI_0}{dz} = -\bar{k}(1 - \bar{a}\bar{g})I_1 \tag{6a}$$

Integrating (1) with respect to $d(\cos \theta)$ and $d\phi$ over $-1 \le \cos \theta \le 1$ and $0 \le \phi \le 2\pi$ yields

$$\frac{dI_1}{dz} = -3\bar{k}(1 - \bar{a})(I_0 - T) \tag{6b}$$

where $\bar{k}$ is the extinction coefficient of an ensemble of spherical particles or it may be $(k_h + k_v)/2$ for an ensemble of aspherical particles whose volumes are equal to those of the spherical particles. The quantities $\bar{a}$ and $\bar{g}$ are readily obtained from Mie theory. The downward flux at the top of the cloud determines the upper boundary condition

$$\left(I_0 - \frac{2}{3} I_1\right)_{z=z^*} = 2.7°K \tag{7a}$$

The upward flux at the bottom of the cloud is

$$\left(I_0 + \frac{2}{3} I_1\right)_{z=0} = \bar{\varepsilon}T_0 + (1 - \bar{\varepsilon})\left(I_0 - \frac{2}{3} I_1\right)_{z=0} \tag{7b}$$

and

$$\bar{\varepsilon} = \int_0^1 [\varepsilon_h(\theta) + \varepsilon_v(\theta)] \cos \theta \, d(\cos \theta) \tag{8}$$

A common approach to the solutions of (6) is to differentiate (6b) and insert that function into (6a). A straightforward second-order differential equation in I_0 ensues when $\bar{k}$, $\bar{a}$, and $\bar{g}$ are independent of height. However, these parameters do, in fact, vary abruptly with height because of phase transitions from ice to water. These transitions cause large changes in $\bar{k}(1 - \bar{a}\bar{g})$ and $3\bar{k}(1 - \bar{a})$ in (6a) and (6b) so that the numerical solution of any second-order differential equation becomes unstable. Therefore, the following algorithm to solve (6a), (6b), (7a), and (7b) numerically was developed.

The atmosphere is stratified in the manner shown in Figure 1. Equation (6a) and (6b) may be written in finite difference form:

$$I_{0,i+1} - I_{0,i} = -E_{i+1}I_{1,i+1} \qquad 0 \le i \le n - 1 \tag{9a}$$

$$I_{1,i+1} - I_{1,i} = -F_i(I_{0,i} - T_i) \qquad 0 \le i \le n \tag{9b}$$

where

$$E_i = \bar{k}_i \Delta z(1 - \bar{a}_i\bar{g}_i)$$

is defined at the dashed levels, and

$$F_i = 3\bar{k}_i \Delta z(1 - \bar{a}_i)$$

and T_i are defined at the solid levels of Figure 1. The boundary conditions become

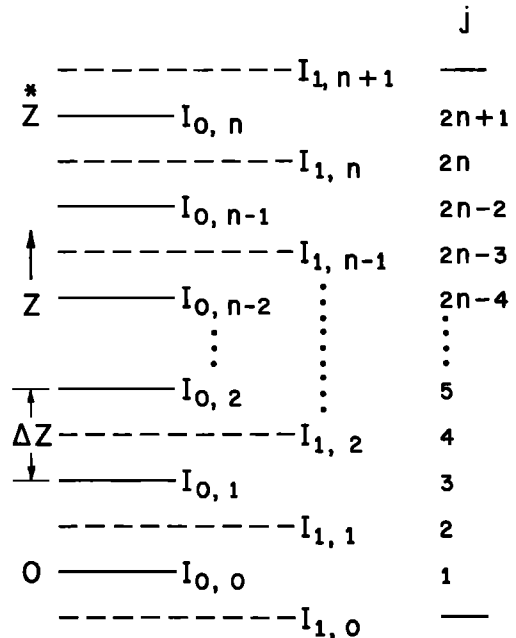$$I_{0,n} - \frac{1}{3} [I_{1,n+1} + I_{1,n}] = 2.7°K \tag{9c}$$

Fig. 1. Schematic figure showing incrementation of the numerical algorithm used to solve (9).

$$I_{0,0} + \left[\frac{2 - \bar{\varepsilon}}{3\bar{\varepsilon}}\right](I_{1,0} + I_{1,1}) = T_0 \qquad (9d)$$

Equations (9c) and (9d) thus define $I_{1,0}$ and $I_{1,n+1}$ so that (9a) and (9b) can be reduced to n equations in $I_{0,i}$ and $n + 1$ equations in $I_{1,i}$. Equations (9) may be rewritten in a vector form that is compatible with the scheme shown in Figure 1, namely:

$$\mathbf{A} \cdot \bar{\mathbf{I}} = \bar{\mathbf{T}} \qquad (10a)$$

In that case,

$$\bar{\mathbf{I}} = (\mathbf{i}_1, \mathbf{i}_2, \ldots, \mathbf{i}_{2n+1}) \qquad (10b)$$

such that

$$\mathbf{i}_j = I_{0,i} \qquad j = 2i + 1 \qquad 0 \le i \le n$$
$$\mathbf{i}_j = I_{1,i} \qquad j = 2i \qquad 1 \le i \le n$$

and

$$\bar{\mathbf{T}} = (\mathbf{t}_1, \mathbf{t}_2, \ldots, \mathbf{t}_{2n+1}) \qquad (10c)$$

where

$$\mathbf{t}_1 = \left(\frac{3\bar{\varepsilon}}{2 - \bar{\varepsilon}} + F_0\right)\frac{T_0}{2}$$

$$\mathbf{t}_{j'} = F_i T_i \qquad j' = 2i + 1 \qquad 1 \le i \le n - 1$$

$$\mathbf{t}_{j'} = 0 \qquad j' = 2i \qquad 1 \le i \le n$$

and

$$\mathbf{t}_{2n+1} = \tfrac{1}{2}F_n T_n + 4.05$$

and where $\mathbf{A}$ is a $(2n + 1) \times (2n + 1)$ dimensional tridigaonal matrix with components

$$\mathbf{a}_{j',j} = 0 \qquad |j - j'| > 1$$

$$\mathbf{a}_{j',j} = -1 \qquad j - j' = -1$$

$$\mathbf{a}_{j',j} = 1 \qquad j - j' = 1$$

$$\mathbf{a}_{j,j} = E_{i+1} \qquad j = 2i \qquad 1 \le i \le n - 1$$

$$= F_i \qquad j = 2i + 1 \qquad 1 \le i \le n - 1$$

$$\mathbf{a}_{1,1} = \frac{1}{2}\left(\frac{3\bar{\varepsilon}}{2 - \bar{\varepsilon}} + \Phi_0\right)$$

$$\mathbf{a}_{2n+1,2n+1} = \frac{1}{2}(3 + F_n)$$

We confine our attention to the upwelling radiances at $\theta = 50°$, the typical viewing angles of the Nimbus 7 and DMSP satellite radiometers. The analysis up to this point has regarded the hydrometeors as spherical; however, we will solve (1) and employ extinction coefficients k_p appropriate for nonspherical particles. The radiance, then, is

$$I_p(z = z^*, \theta = 50°)$$

$$= \varepsilon_p(50°)T_0 \exp\left[-\int_0^{z^*} k_p(z')\, dz'/\cos 50°\right]$$

$$+ [1 - \varepsilon_p(50°)]I_p(z = 0, \theta = 130°)$$

$$\cdot \exp\left[-\int_0^{z^*} k_p(z')\, dz'/\cos 50°\right]$$

$$+ \int_0^{z^*} J(z, \theta = 50°)k_p(z)$$

$$\cdot \exp\left[-\int_z^{z^*} k_p(z')\, dz'/\cos 50°\right] dz/\cos 50° \qquad (11)$$

where

$$I_p(z = 0, \theta = 130°) = \int_0^{z^*} J(z, \theta = 130°)k_p(z)$$

$$\cdot \exp\left[-\int_0^z k_p(z')\, dz'/\cos 50°\right] dz/\cos 50°$$

and

$$J(z, \theta) = (1 - \bar{a})T + \bar{a}(I_0 + \bar{g}I_1 \cos \theta)$$

Note that this source function is independent of polarization.

The integrand in the last term of (11) is designated as $W(z)$. Profiles of $W(z)$ reveal the contributions of different parts of the atmosphere to the upwelling radiances.

2b. Extinction Coefficients of Hydrometeors

The radiative properties of spherical hydrometeors were obtained from Mie theory. The refractive indices of water and ice prescribed in the review article of *Ray* [1972] were utilized in the Mie calculations. The hydrometeor size distribution is assumed to be that of *Marshall and Palmer* [1948], where $n_0 = 1.6 \times 10^4 \text{m}^{-3}\text{mm}^{-1}$, and $\Lambda = 8.2\, R^{-0.21}$, and where R is the rainfall rate in mm/h irrespective of the phase of the hydrometeors, i.e.,

$$\frac{dn}{dr} = n_0 \exp(-\Lambda r) \qquad (12)$$

The parameters describing the interaction of radiation with the polydisperse hydrometeors were obtained by integrating the product of the Mie parameters and the size distribution given by (12).

The albedo for single scattering, the asymmetry factor, and the extinction coefficient resulting from ice and 20°C water spherical hydrometeors can be respectively approximated by

$$a = AR^\alpha \qquad (13a)$$

$$g = G_0 R^\gamma \qquad (13b)$$

or

$$g = G_1 + G_2 R + G_3 \log_{10} R \qquad (13c)$$

$$k = KR^\kappa \qquad (13d)$$

The extinction coefficient k is in units of km^{-1} and R is in mm/h. The parameters A, α, G_0, G_1, G_2, G_3, γ, K, and κ are presented in Table 1.

The quantities ultimately used in the radiative transfer equation also incorporate the effect of gaseous absorption so that

$$\bar{a} = ka/\bar{k} \qquad (14a)$$

$$\bar{g} = g \qquad (14b)$$

$$\bar{k} = k + k_{O_2} + k_{H_2O} \qquad (14c)$$

where k_{O_2} and k_{H_2O} are absorption coefficients of oxygen and water vapor.

TABLE 1. Radiative Transfer Parameters of Hydrometeors Determined at 130° with Respect to Nadir

	Frequency, GHz						
	6.6	10.7	18.0	21.0	37.0	85.6	183.0
Water, 20°C							
a: Albedo for Single-Scattering, Spherical Hydrometeors							
$(100 \cdot A)/\alpha$	5.22/.017	6.15/.110	7.99/.285	11.9/.239	30.7/.108	45.3/0.041	47.3/.027
g: Asymmetry Factor, Spherical Hydrometeors							
$(100 \cdot G_0)/\gamma$	—	—	—	—	—	13.3/0.234	39.6/0.111
$(100 \cdot G_1)$	4.49	10.36	0.183	−2.77	−4.43	—	—
$(100 \cdot G_2)$	−0.119	−0.048	0.089	0.086	0.066	—	—
$(100 \cdot G_3)$	6.78	−9.13	−8.89	−6.00	2.60	—	—
$k(km^{-1})$: *Extinction Coefficient, Spherical Hydrometeors*							
$(100 \cdot K)/\kappa$	0.052/1.30	0.371/1.17	1.73/1.04	2.48/1.02	9.48/0.893	35.2/0.706	50.3/0.630
$k_h(km^{-1})$: *Horizontally Polarized Extinction Coefficient, Aspherical Hydrometeors*							
$(100 \cdot K_h)/\kappa_h$	0.061/1.30	0.377/1.18	1.58/1.08	2.33/1.05	9.04/0.916	—	—
$k_v(km^{-1})$: *Vertically Polarized Extinction Coefficient, Aspherical Hydrometeors*							
$(100 \cdot K_v)/\kappa_v$	0.058/1.28	0.353/1.17	1.52/1.06	2.23/1.03	8.41/0.911	—	—
Ice							
a: Albedo for Single-Scattering, Spherical Hydrometeors							
$(100 \cdot A)/\alpha$	56.6/0.056	83.2/0.029	88.5/0.027	98.6/0.002	100/0	100/0	100/0
g: Asymmetry Factor, Spherical Hydrometeors							
$(100 \cdot G_1)$	0.327	0.852	2.41	3.28	10.71	40.10	53.45
$(100 \cdot G_2)$	0.008	0.020	0.058	0.084	0.029	−0.140	−0.040
$(100 \cdot G_3)$	0.541	1.41	4.00	5.43	15.90	11.36	0.894
$k(km^{-1})$: *Extinction Coefficient, Spherical Hydrometeors*							
$(100 \cdot K)/\kappa$	0.001/1.21	0.004/1.27	0.029/1.27	0.052/1.28	0.412/1.28	10.3/0.932	43.6/0.681
$k_h(km^{-1})$: *Horizontally Polarized Extinction Coefficient, Aspherical Hydrometeors*							
$(100 \cdot K_h)/\kappa_h$	0.006/1.13	0.012/1.16	0.041/1.26	0.073/1.25	0.762/1.18	—	—
$k_v(km^{-1})$: *Vertically Polarized Extinction Coefficient, Aspherical Hydrometeors*							
$(100 \cdot K_v)/\kappa_v$	0.004/1.15	0.008/1.21	0.028/1.28	0.051/1.27	0.450/1.26	—	—

When aspherical hydrometeors were considered, the albedo for single scattering and asymmetry factors for spherical hydrometeors with the same volume were retained. Only the extinction coefficients were altered to incorporate effects resulting from the deformation of the hydrometeors.

In the case of aspherical particles the extinction cross section is

$$Q_p = -(4\pi/\ell) \, Im \, [f_p(0, \theta)] \qquad (15)$$

where $\ell = 2\pi/\lambda$ and $f_p(0, \theta)$ is the forward scattering amplitude as defined by Oguchi [1983] for vertically (v) and horizontally (h) polarized waves incident at an angle θ to the symmetry axis of the hydrometeors. Because of aerodynamic forces, the symmetry axis is in the vertical for oblate ellipsoids. The viewing angle of the satellite-borne radiometers defines $\theta = 50°$.

The data of Oguchi and Hosoya [1974] was used for aspherical liquid raindrops. The extinction coefficient k_p was obtained by numerically integrating the product of the extinction cross section and the Marshall-Palmer size distribution. Oguchi and Hosoya only presented scattering amplitudes for drops with $\bar{r} \geq 0.025$ cm. Therefore, it was necessary to account for the effect of the smaller, less deformed drops with Mie theory.

The frequencies of the present study are not identical to those considered in the Oguchi and Hosoya study. Therefore, we interpolated the results for frequencies less than 34.8 GHz. Our estimates for the 37.0-GHz scattering amplitude were obtained by extrapolating the data of Oguchi and Hosoya from 34.8 to 37.0 GHz. The temperature dependence of the extinc-

tion coefficient for aspherical raindrops was obtained by scaling the Oguchi and Hosoya results at 20°C with the ratio of Mie theory results at various temperatures i.e.,

$$k_p(T°C) = k_p(20°C) \cdot k(T°C)/k(20°C) \qquad (16)$$

The polarized extinction coefficients of aspherical ice hydrometeors were obtained in a somewhat more complex fashion:

The hydrometeors with volumetric equivalent radii $\bar{r} < 0.1$ cm were assumed to be oblate ellipsoidal approximations to plates whose shape was defined by

$$2b = 1.41 \times 10^{-2}(2a)^{0.474} \qquad (17)$$

where a and b are the semimajor and semiminor axes, respectively; all dimensions are given in centimeters [see Prupacher and Klett, 1980]. Rayleigh-Ganz theory was employed to derive the extinction cross sections of these small monodisperse hydrometeors [see van de Hulst, 1981]. The extinction coefficient of the ensemble of particles was then obtained by integrating the product of the Marshall-Palmer size distribution and the Rayleigh-Ganz extinction cross sections over equivalent radii from $0 < \bar{r} < 0.1$ cm.

The extinction cross sections for ice hydrometeors with equivalent radii between $0.1 \leq \bar{r} \leq 0.2$ cm. were obtained from the scattering amplitudes of ice hydrometeors that were presented by Evans and Holt (1977). That data could not be applied directly to the cases that are considered in this study. Accordingly, those data were plotted in the form:

$$\ell Im[f(0, 0)] = \Upsilon(\ell\bar{r}) \qquad (18a)$$

$$\ell Im[f_h(0, \pi/2)] = \Phi(\ell \bar{r}) \qquad (18b)$$

and

$$\ell Im[f_v(0, \pi/2)] = \Psi(\ell b) \qquad (18c)$$

as suggested by *Holt and Evans* [1980] for water hydrometeors. In that case Υ, Φ, and Ψ were empirically observed functions of $\bar{r}$, the radius of a sphere whose volume is that of the ellipsoid, and b, the semiminor axis of the ellipsoids. The wave number is ℓ, and the forward scattering amplitudes are $f_p(0, \theta)$ as in (15). The scattering amplitudes at the SMMR frequencies were obtained by interpolating the functions Υ, Φ, and Ψ. The scattering amplitudes for radiation incident at $\theta = 50°$ to the hydrometeor symmetry axis were obtained from the relationship

$$f_p(0, \theta) = f(0, 0) \cos^2 \theta + f_p(0, \pi/2) \sin^2 \theta \qquad (19)$$

put forth by *Uzunoglu et al.* [1977]. These scattering amplitudes were incorporated in (15) to yield the extinction cross sections. The product of the Marshall-Palmer size distribution and the extinction cross section was integrated between equivalent radii of $0.1 < \bar{r} < 0.2$ cm to provide yet a further contribution to the extinction coefficient. Estimates of k_p could not be derived for frequencies in excess of 37 GHz because Evans and Holt did not calculate the forward scattering amplitude for the appropriately large-size parameters.

Ice particles with $\bar{r} > 0.2$ cm are small hailstones. These may frequently assume a spherical shape. Therefore, Mie theory was used to compute the extinction coefficient in this size range.

3. COMPUTATIONAL RESULTS AND DISCUSSION

3a. Scalar Source Function Approximation

The first test determined whether a scalar source function could be applied to a problem that considered polarization. Therefore, the present model was run initially on the assumption that liquid hydrometeor drops were spherical so that $k_h = k_v = \bar{k}$. The underlying surface was assumed to be calm pure water so that $\varepsilon_v \neq \varepsilon_h$. The parameters of the 37 GHz model of *Weinman and Guetter* [1977] were inserted into the present model. The scattering phase matrix in that paper was a Rayleigh phase matrix; however, the present phase function was assumed to be isotropic i.e., $\bar{g} = 0$. Table 2 summarizes the parameters used in this test of the model. Table 3 presents a comparison between the 37-GHz brightness temperatures at

TABLE 2. Parameters Used to Test Validity of Scalar Source Function

T^*	258°K	(cloud-top temperature)
T	288°K	(surface temperature)
z^*	4.57 km	(cloud top altitude) $\Gamma = 6.56°C/km$
$(k_{O_2} + k_{H_2O})z^*$	0.07	(optical thickness of gaseous absorbers)
$\cos \theta$	0.6612	
$\bar{\varepsilon}$	0.461	(cosine-weighted average emission coefficient of calm water)
$\varepsilon_v(\theta)$	0.605	(polarized emission coefficients
$\varepsilon_h(\theta)$	0.333	of calm water at 37 GHz)

	Rainfall Rate, mm/h				
	2	4	8	16	32
$\bar{a}$	0.23	0.27	0.33	0.37	0.40
$\bar{k}(km^{-1})$	0.155	0.291	0.567	1.12	2.23

TABLE 3. Comparison of the Present Model Brightness Temperatures With Those of *Weinman and Guetter* [1977]

		Rainfall Rate, mm/h				
		2	4	8	16	32
I_h	PM	234.4	248.7	244.1	237.3	232.6
	WG	233.7	247.3	242.9	236.1	232.4
I_v	PM	245.7	250.8	244.2	237.3	232.6
	WG	247.2	251.7	245.1	238.5	235.4

Values in °K; PM, present model; WG, *Weinman and Guetter* [1977].

$\theta = 48.6°$, derived from the more rigorous model that utilized a Rayleigh phase matrix, and the present simplified model that assumed a scalar isotropic phase function. The two methods agree within 0.2 to 2.8°C.

3b. Spherical Ice, Combined Phase, and Water Hydrometeors

The second test considered the effect of spherical rain, combined phase, and ice hydrometeors. Precipitating systems are considered over land and ocean. The surface temperature is maintained at 298°K. The temperature profile is representative of summer temperate or tropical conditions, i.e., 10°C was added to a U.S. Standard Atmosphere below the tropopause. The water vapor profile was that of the U.S. Standard Atmosphere. The extinction coefficient of oxygen, k_{O_2}, is obtained from the work of *Rosenkranz* [1975], and the extinction coefficient of water vapor, k_{H_2O}, is obtained from *Staelin* [1966].

Seven rainfall rate profiles are shown in Figure 2 along with the average water content of eight heavy thunderstorms computed from the radar measurements of *Geotis* [1971]. The hydrometeors were assumed to be liquid up to the 0°C isotherm at 3.87 km in a combination of phases between 3.87 and 9.27 km, the $-35°C$ isotherm, and all ice above 9.27 km. Specifically, the mass of hydrometeors in the transition zone were represented by
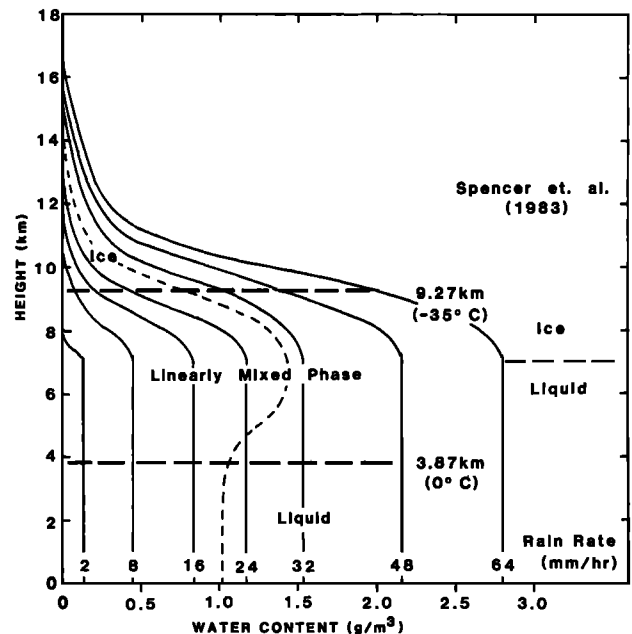

Fig. 2. Schematic model of the distribution of hydrometeors with various phases as a function of height. The two-phase model used in the study of *Spencer et al.* [1983a] is shown at the right. This figure also illustrates the profiles of precipitating water used in (11). The dashed profile is due to *Geotis* [1971].
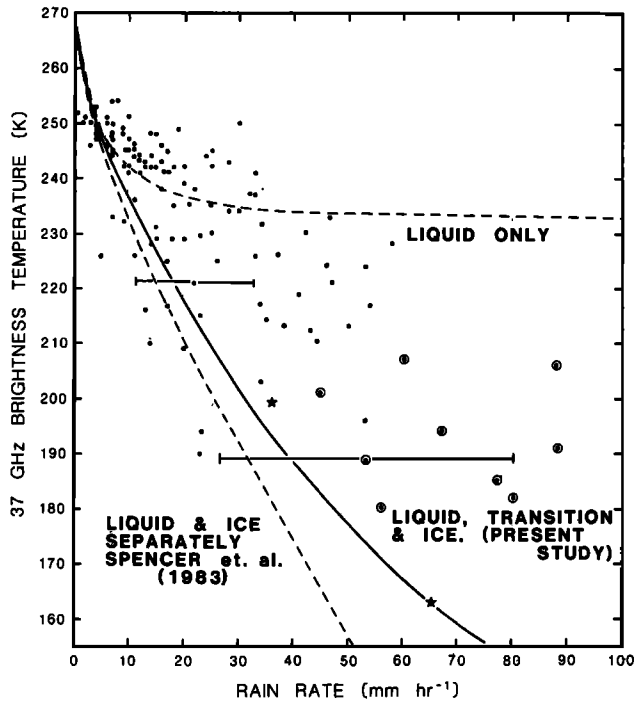
Fig. 3. The rainfall rates inferred from radar compared to the horizontally polarized brightness temperatures measured by the 37-GHz channel of the SMMR. The various dots are measurements described more comprehensively by Spencer et al. [1983a]. The dashed lines present the results of a model that contains liquid precipitation only and a model that consists of water and ice hydrometeors. The solid line presents the results obtained from the present model.

$$IWC = \left[\frac{z - 3.87}{5.40}\right] TWC \qquad (20a)$$

$$3.87 \le z \le 9.27 \text{ km}$$

$$LWC = \left[\frac{9.27 - z}{5.40}\right] TWC \qquad (20b)$$

where IWC, LWC, and TWC were the ice water content, liquid water content, and total water content (shown in Figure

2), respectively. A similar model that neglected the coexistence of both types of hydrometeors was described by Spencer et al. [1983a].

Figure 3 presents a comparison between the 37-GHz results of the present computation and the measurements and earlier theoretical results presented by Spencer et al. [1983a]. Most clouds are only partially capped by ice hydrometeors, and many precipitating clouds are not sufficiently large to fill the 37-GHz SMMR radiometer footprint so that the measured brightness temperatures may be expected to exceed those predicted by the present model.

Microwave brightness temperatures were also computed for radiances at five SMMR frequencies, the 85.6-GHz SSM/I frequency, and the 183-GHz frequency that has been proposed for a water vapor monitoring instrument. A 183-GHz radiometer is expected to provide better spatial resolution than the 21-GHz channel that is now a part of the SMMR.

The results obtained from the model are in Table 4. Note that no difference in brightness temperatures at the two polarizations occur when spherical hydrometeors exist over land. The polarized radiances from clouds over water are due to the polarized emissivity of the sea. The underlying surface is obscured by heavy rain so that polarization effects are eliminated. The model suggests that brightness temperatures over land diminish monotonically with rainfall rate; however, the brightness temperatures over water appear to be double-valued functions. Polarization is least for the heavy rainfall rates over the sea, so that it should be possible to separate the two values of rainfall rate that correspond to a given brightness temperature.

In order to illustrate the importance of the contributions of various layers in precipitating clouds to the derived brightness temperatures the quantities $W(z)$, defined in (11), are shown in Figures 4, 5, and 6. The height of the precipitation column top rises with increasing rainfall rates so that $W(z)$ assumes finite values at higher altitudes as the surface rainfall rate increases. It is evident from these figures that 183- and 85-GHz radiometers will be sensitive to the upper 3-5 km of a cloud that contains ice hydrometeors. The underlying liquid hydrometeors can be expected to have only a slight effect on those brightness temperatures. However, the ice concentration may

TABLE 4. Brightness Temperatures Emerging at 130° From Precipitating Clouds Containing Spherical Hydrometeors

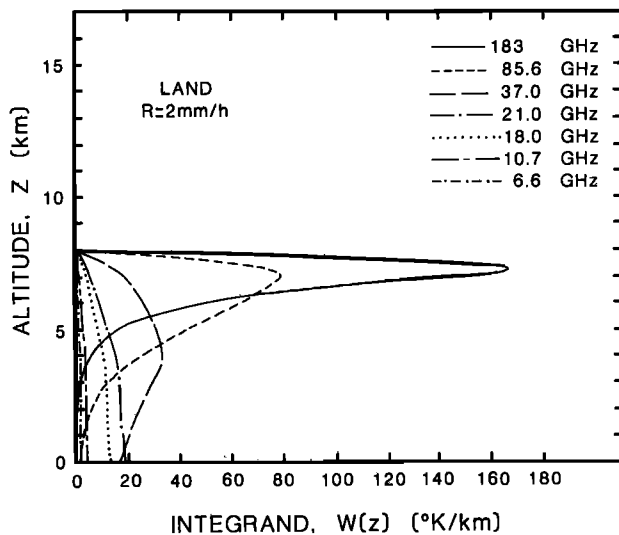| Rainfall Rate, mm/h	Frequency, GHz						
	6.6 I_h/I_v	10.7 I_h/I_v	18.0 I_h/I_v	21.0 I_h/I_v	37.0 I_h/I_v	85.6 I_h/I_v	183.0 I_h/I_v
	Over Land: $\varepsilon_h(130°) = \varepsilon_v(130°) = \bar{\varepsilon} = 0.9$						
2	269.3	270.8	273.7	274.6	262.6	247.3	257.2
4	269.9	272.6	273.7	271.8	252.6	238.9	258.0
8	271.0	274.6	267.9	261.9	240.8	225.4	240.6
16	273.2	274.9	258.7	251.9	229.0	201.0	197.4
32	275.6	268.1	245.1	237.0	198.8	121.1	89.5
48	275.4	261.0	237.1	227.8	179.6	99.4	69.2
64	274.2	256.2	229.3	218.3	165.3	80.3	55.7
	Over Water: $\varepsilon_h(130°) = 0.333$, $\varepsilon_v(130°) = 0.605$ and $\bar{\varepsilon} = 0.461$						
2	88.4/160.4	109.6/175.0	168.9/213.1	200.6/232.2	247.3/253.9	247.3	257.2
4	96.3/165.4	136.5/191.5	215.0/239.4	238.4/252.4	251.0/251.6	238.9	258.0
8	113.5/176.1	183.6/220.2	251.5/258.1	255.8/258.2	240.8	225.4	240.6
16	147.1/197.1	238.0/252.6	257.3/257.8	251.6/251.7	229.0	201.0	197.4
32	203.3/231.8	263.1/265.0	245.1	237.0	198.8	121.1	89.5
48	237.1/252.1	260.3/260.6	237.1	227.8	179.6	99.4	69.2
64	255.0/262.5	256.1/256.2	229.3	218.3	165.3	80.3	55.7

Values expressed in °K.

Fig. 4. The weighting functions that represent the integrands in (11) for various frequencies at a surface rainfall rate of 2 mm/h for a precipitating cloud over land.

Fig. 6. Same as Figure 4 for a surface rainfall rate of 64 mm/h.

be expected to be correlated to the rainfall rate so that it may be possible to infer rainfall rates from these higher-frequency channels by indirect means. Moreover, the improved spatial resolution of the high-frequency images should permit enhancement of the resolution of lower-frequency images by means of the technique described by *Olson et al.* [1983]. Brightness temperatures measured at frequencies of the present SMMR are increasingly sensitive to the lower liquid precipitation layers as their frequency diminishes.

Table 4 shows that the horizontally and vertically polarized brightness temperatures obtained from this model approach identical magnitudes as the rainfall rates increase. However, *Spencer et al.* [1983b] noted that $I_v - I_h = 12 \pm 2°K$ at 37 GHz, even for high rainfall rates. Therefore, we will investigate the effect of nonspherical hydrometeors on the emerging radiances.

3c. Spherical Ice, Combined Phase, and Aspherical Water Hydrometeors

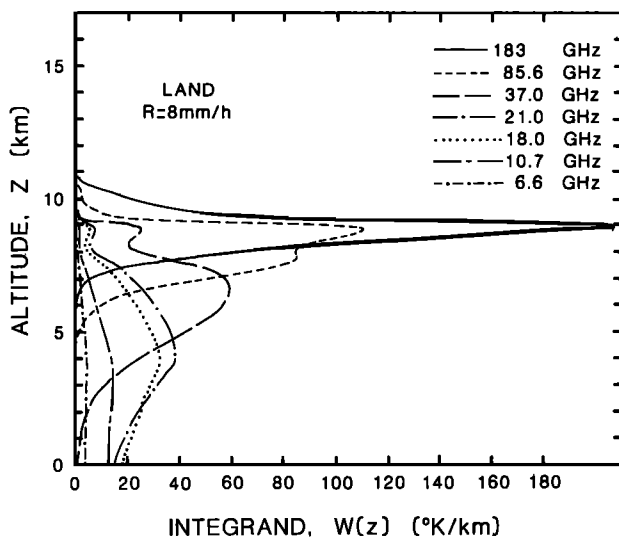The cause of the observed net residual polarization was first

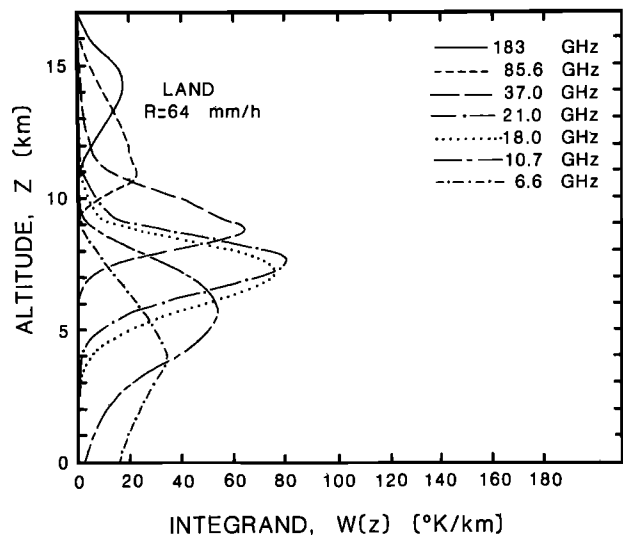Fig. 5. Same as Figure 4 for a surface rainfall rate of 8 mm/h.

sought from the deformed large water drops known to occur at high rainfall rates. The polarized extinction coefficients cited in section 2b were employed in (11) to compute radiances at various SMMR frequencies. The results of these computations are presented in Table 5.

Table 5 illustrates that differences in the polarized brightness temperatures of radiances emerging from all precipitation over land and heavy precipitation over water are of the order of a few degrees kelvin. This is nearly an order of magnitude too small to account for the observations of *Spencer et al.* [1983b]. Therefore, an explanation for this discrepancy is sought in the radiative properties of aspherical ice hydrometeors.

3d. Aspherical Ice, Combined Phase, and Water Hydrometeors

The results displayed in Table 6 are similar to those shown in Tables 4 and 5. The data summarized in Table 6 shows that ice hydrometeors reduce the brightness temperatures at both polarizations; however, the horizontally polarized radiances are significantly reduced at surface rainfall rates in excess of 48 mm/h. The differences in brightness temperatures, $I_v - I_h$, at heavy rainfall rates is 11°K for 37.0-GHz radiances. This difference drops to between 5° and 6°K at 21.0 GHz, and it continues to diminish monotonically as the frequencies diminish. The computed magnitudes of $I_v - I_h$ are in reasonable agreement with the measurements that *Spencer et al.* [1983b] and R. W. Spencer (private communication, 1984) found at 37.0 and 21.0 GHz. However the measured values of $I_v - I_h$ then increase at frequencies less than 18.0 GHz. The discrepancy between the measured and computed values of $I_v - I_h$ at the lower frequencies may be attributed to the fact that the lower-frequency SMMR footprints are large and widely separated, and centers of the horizontally and vertically polarized footprints are not colocated.

It should be noted that the 0.1-cm volumetric cutoff radius separating the small aspherical ice hydrometeors from the large spherical hydrometeors was chosen somewhat arbitrarily. The shapes of ice hydrometeors are a sensitive function of the history of their evolution; the 0.1-cm cutoff radius was selected because we had no information regarding hydrometeor evolution. A smaller 0.08-cm cutoff radius would have reduced $I_v - I_h$ to 8.4°K and 4.5°K at 37.0 GHz and 21.0

TABLE 5. Brightness Temperatures Emerging at 130° From Precipitating Clouds Containing Spherical Ice Particles and Deformed Water Drops

Rainfall Rate, mm/h	Frequency, GHz				
	6.6 I_h/I_v	10.7 I_h/I_v	18.0 I_h/I_v	21.0 I_h/I_v	37.0 I_h/I_v
Over Land: $\varepsilon_h(130°) = \varepsilon_v(130°) = \bar\varepsilon = 0.9$					
2	269.3/269.2	270.7/270.6	273.5/273.4	274.4	262.5/263.3
4	269.8/269.7	272.5/272.3	273.6/273.7	271.7/272.0	252.1/253.3
8	271.0/270.8	274.8/274.6	267.6/268.4	261.5/262.7	240.1/241.3
16	273.4/273.1	274.7/275.0	257.6/258.9	251.0/252.3	228.7/229.7
32	276.1/275.9	266.7/267.9	243.9/245.2	236.0/237.2	198.7/199.3
48	275.8/276.1	259.9/261.2	236.5/237.6	227.4/228.5	180.1/180.2
64	274.5/275.3	255.2/256.5	228.4/229.7	217.6/218.8	164.9/165.3
Over Water: $\varepsilon_h(130°) = 0.333$, $\varepsilon_v(130°) = 0.605$ and $\bar\varepsilon = 0.461$					
2	87.1/159.3	107.2/172.7	164.6/208.8	196.4/228.1	245.2/252.3
4	94.2/163.4	134.6/188.5	213.9/236.4	237.5/250.2	250.2/251.8
8	111.1/173.0	184.5/217.5	252.1/257.5	255.8/258.4	240.1/241.2
16	146.6/193.4	241.0/251.7	256.6/258.0	250.8/252.1	228.7/229.7
32	205.6/228.3	262.9/264.7	243.9/245.2	236.0/237.2	198.7/199.3
48	239.9/249.7	259.5/260.8	236.5/237.6	227.4/228.5	180.1/180.2
64	257.1/261.2	255.2/256.5	228.4/229.7	217.6/218.8	164.9/165.3

Values expressed in °K.

GHz, respectively, at rainfall rates in excess of 48 mm/h. This study suggests that dual polarization multifrequency radiometers might provide useful insights regarding the physics of hail laden clouds.

4. DISCUSSION AND CONCLUSIONS

A numerical algorithm based on Eddington's second approximation to the equation of radiative transfer was developed to compute the radiances with horizontal and vertical polarization that emerge from precipitating clouds. This algorithm yields a rapid solution to problems pertaining to clouds with vertically inhomogeneous structure. Precipitating clouds containing liquid, mixtures of phases, and ice hydrometeors could thus be modeled.

The extinction coefficients of aspherical drops observed at 50° with respect to their axis of symmetry were computed from the data of Oguchi and Hosoya [1974]. The drop size distributions were assumed to be described by Marshall-Palmer distributions. Extinction coefficients of ellipsoidal ice hydrometeors with volumetric radii <0.1 cm and shapes suggested by Prupacher and Klett [1980] were also computed from the methods of Rayleigh-Ganz and Evans and Holt [1977] for frequencies up to 37 GHz.

Brightness temperatures of radiances that SSM/I and SMMR can measure were presented as functions of rainfall rate. The presence of ice hydrometeors markedly depressed the brightness temperatures. Heavy rain events can thus be measured over land to the extent that ice concentrations are correlated to total precipitation. The altitudes from which the various radiances emanate at several rainfall rates were also presented to provide insight regarding the response of various radiometer channels to rainfall intensities. It was shown that the lower-frequency radiances respond more to water drops at

TABLE 6. Brightness Temperatures Emerging at 130° From Precipitating Clouds Containing Deformed Ice and Water Hydrometeors

Rainfall Rate, mm/h	Frequency, GHz				
	6.6 I_h/I_v	10.7 I_h/I_v	18.0 I_h/I_v	21.0 I_h/I_v	37.0 I_h/I_v
Over Land: $\varepsilon_h(130°) = \varepsilon_v(130°) = \bar\varepsilon = 0.9$					
2	269.3/269.2	270.7/270.6	273.5/273.4	274.4/274.4	262.3/263.3
4	269.8/269.7	272.5/272.3	273.6/273.7	271.6/272.0	251.7/253.4
8	271.0/270.8	274.8/274.6	267.4/268.4	261.3/262.7	239.2/241.5
16	273.4/273.1	274.6/275.0	257.3/258.9	250.5/252.4	225.9/229.9
32	275.8/275.7	266.1/267.5	242.4/245.2	233.7/237.4	188.8/198.8
48	275.1/275.7	258.9/260.6	234.3/237.7	224.0/228.9	168.1/179.3
64	273.5/274.6	254.0/255.8	225.8/229.9	213.6/219.3	152.7/164.0
Over Water: $\varepsilon_h(130°) = 0.333$, $\varepsilon_v(130°) = 0.605$ and $\bar\varepsilon = 0.461$					
2	87.1/159.3	107.3/172.7	164.7/208.8	196.5/228.1	245.2/252.4
4	94.3/163.4	134.7/188.5	214.1/236.5	237.7/250.2	249.9/251.9
8	111.3/173.1	184.7/217.6	252.1/257.5	255.7/258.4	239.1/241.4
16	147.1/193.6	241.1/251.7	256.2/258.0	250.3/252.2	225.9/229.9
32	206.5/228.6	262.4/264.4	242.4/245.2	233.7/237.4	188.8/198.8
48	240.2/249.7	258.5/260.2	234.3/237.7	224.0/228.9	168.1/179.3
64	256.8/261.0	253.9/255.7	225.8/229.9	213.6/219.3	152.7/164.0

Values expressed in °K.

the bottom of the clouds and the radiances at higher frequencies are more sensitive to ice near the cloud top.

The differences in brightness temperatures of radiances that are horizontally and vertically polarized are $<1°K$ if the raindrops are either spherical or deformed in the manner described by Oguchi [1983]. However, aspherical ice particles can markedly affect the difference in brightness temperatures. A dual polarization multichannel microwave radiometer and a dual polarization radar mounted on a high-altitude aircraft might thus provide considerable insight on clouds that contain hailstones. Since such an aircraft would not be exposed to hail impaction, no special structural modifications would be required.

REFERENCES

Atlas, D., and O. W. Thiele, Precipitation measurements from space, workshop report, NASA Goddard Space Flight Center, Greenbelt, Md., 1981.
Bostian, C. W., and J. E. Allnutt, Ice-crystal depolariztion on satellite-earth microwave radio paths, *Proc IEEE, 126,* 951–960, 1979.
Evans, B. G., and A. R. Holt, Scattering amplitudes and cross polarization of ice particles, *Electron. Lett., 13*(12), 342–344, 1977.
Geotis, S. G., Thunderstorm water content and rain fluxes deduced from radar, *J. Appl. Meteorol., 10,* 1233–1237, 1971.
Holt, A. R., and B. G. Evans, The scattering of millimeter waves by precipitation particles, paper presented at Open Symposium on Effects of the Lower Atmosphere on Radio Propagation at Frequencies Above 1 GHz, URSI, Lennoxville, Canada, 1980.
Huang, R., and K. N. Liou, Polarized microwave radiation transfer in precipitating cloudy atmospheres: Applications to window frequencies, *J. Geophys. Res., 88,* 3885–3893, 1983.
Liou, K. N., *An Introduction to Atmospheric Radiation,* Academic, pp. 392, New York, 1980.
Marshall, J. S., and W. M. Palmer, The distribution of raindrops with size, *J. Meteorol., 5,* 165–166, 1948.
Oguchi, T., Electromagnetic wave propagation and scattering in rain and other hydrometeors, *Proc. IEEE, 71,* 1029–1078, 1983.

Oguchi, T., and Y. Hosoya, Scattering properties of oblate raindrops and cross polarization of radiowaves due to rain, 2, Calculation at microwave and millimeter wave regions, *J. Radio Res. Lab. Jpn., 21,* 191–259, 1974.
Olson, W. S., J. A. Weinman, C. L. Yeh, and R. T. Chin, Distribution of maritime rain determined from multichannel microwave radiometry, paper presented at Fifth Conference on Atmospheric Radiation, Am. Meteorol. Soc., Baltimore, Md., Oct. 31–Nov. 4, 1983.
Prupacher, H. R., and J. D. Klett, *Microphysics of Clouds and Precipitation,* pp. 714, D. Reidel, Hingham, Mass., 1980.
Ray, P. S., Broadband complex refractive indices of ice and water, *Appl. Opt., 11,* 1836–1843, 1972.
Rosenkranz, P. W., Shape of the 5 mm oxygen band in the atmosphere, *IEEE Trans. Antennas Propag., AP-23,* 498–506, 1975.
Spencer, R. W., W. S. Olson, Wu Rongzhang, D. W. Martin, J. A. Weinman, and D. A. Santek, Heavy thunderstorms observed over land by the Nimbus-7 scanning multichannel microwave radiometer, *J. Climat. Appl. Meteorol., 22,* 1041–1046, 1983a.
Spencer, R. W., B. B. Hinton, and W. S. Olson, Nimbus-7 37 GHz radiances correlated with radar rain rates over the Gulf of Mexico, *J. Climat. Appl. Meteorol., 22,* 2095–2099, 1983b.
Staelin, D. H., Measurements and interpretation of the microwave spectrum of the terrestrial atmosphere near 1-cm wavelength, *J. Geophys. Res., 71,* 2875–2881, 1966.
Uzunoglu, N. K., and A. R. Holt, The scattering of electromagnetic radiation from dielectric scatterers, *J. Phys. A: Math. Gen., 10,* 413–424, 1977.
van de Hulst, H. C., *Light Scattering by Small Particles,* pp. 470, Dover, New York, 1981.
Weinman, J. A., and P. J. Guetter, Determination of rainfall distributions from microwave radiation measured by the Nimbus-6 ESMR, *J. Appl. Meteorol., 16,* 437–442, 1977.
Weinman, J. A., and R. Davies, Thermal microwave radiances from horizontally finite clouds of hydrometeors, *J. Geophys. Res., 83,* 3099–3107, 1978.
Wilheit, T. T., A. T. C. Chang, J. L. King, E. B. Rodgers, R. A. Nieman, B. M. Krupp, A. S. Milman, J. S. Stratigos, and H. Siddalingaiah, Microwave radiometric observations near 19.35, 92, and 183 GHz of precipitation in tropical storm Cora, Ocean emissivity algorithm, *J. Appl. Meteorol., 21,* 1137–1145, 1982.

J. A. Weinman, Space Science and Engineering Center, University of Wisconsin, Madison, WI 53706.
R. Wu, Central Meteorological Bureau, Beijing, People's Republic of China.